Dependence of coronal mass ejections on the morphology and toroidal flux of their source magnetic flux ropes

J. H. Guo, L. Linan, S. Poedts, Y. Guo, B. Schmieder, A. Lani, Y. W. Ni, M. Brchnelova, B. Perri, T. Baratashvili, et al.

A&A, 690, A189 (2024)
https://doi.org/10.1051/0004-6361/202449731

Astronomy & Astrophysics

Dependence of coronal mass ejections on the morphology and toroidal flux of their source magnetic flux ropes

J. H. Guo[1,2], L. Linan[1], S. Poedts[1,3,⋆], Y. Guo[2], B. Schmieder[1,4], A. Lani[1], Y. W. Ni[2], M. Brchnelova[1], B. Perri[5,1], T. Baratashvili[1], S. T. Li[6,7], and P. F. Chen[2,⋆]

[1] Centre for Mathematical Plasma Astrophysics, Department of Mathematics, KU Leuven, Celestijnenlaan 200B, B-3001 Leuven, Belgium
[2] School of Astronomy and Space Science and Key Laboratory of Modern Astronomy and Astrophysics, Nanjing University, Nanjing 210023, China
[3] Institute of Physics, University of Maria Curie-Skłodowska, ul. Marii Curie-Skłodowskiej 1, 20-031 Lublin, Poland
[4] LESIA, Observatoire de Paris, CNRS, UPMC, Université Paris Diderot, 5 place Jules Janssen, 92190 Meudon, France
[5] AIM/DAp – CEA Paris-Saclay, Université Paris-Saclay, Université Paris-Cité, Gif-sur-Yvette, France
[6] Key Laboratory of Dark Matter and Space Astronomy, Purple Mountain Observatory, Chinese Academy of Sciences, Nanjing 210023, People's Republic of China
[7] INAF – Turin Astrophysical Observatory, Via Osservatorio 20, 10025 Pino Torinese, (TO), Italy

Received 26 February 2024 / Accepted 12 July 2024

ABSTRACT

Context. Coronal mass ejections (CMEs) stand as intense eruptions of magnetized plasma from the Sun, and they play a pivotal role in driving significant changes of the heliospheric environment. Deducing the properties of CMEs from their progenitors in solar source regions is crucial for space weather forecasting.
Aims. The primary objective of this paper is to establish a connection between CMEs and their progenitors in solar source regions, enabling us to infer the magnetic structures of CMEs before their full development.
Methods. We created a dataset comprising a magnetic flux rope series with varying projection shapes (S-, Z-, and toroid-shaped), sizes, and toroidal fluxes using the Regularized Biot-Savart Laws (RBSL). These flux ropes were inserted into solar quiet regions with the aim of imitating the eruptions of quiescent filaments. Thereafter, we simulated the propagation of these flux ropes from the solar surface to a distance of 25 $R_\odot$ with our global coronal magnetohydrodynamic (MHD) model COCONUT.
Results. Our parametric survey revealed significant impacts of source flux ropes on the consequent CMEs. Regarding the flux-rope morphology, we find that the projection shape (e.g., sigmoid or torus) can influence the magnetic structures of CMEs at 20 $R_\odot$, albeit with minimal impacts on the propagation speed. However, these impacts diminish as source flux ropes become fat. In terms of toroidal flux, our simulation results demonstrate a pronounced correlation with the propagation speed of CMEs as well as the successfulness in erupting.
Conclusions. This work builds the bridge between the CMEs in the outer corona and their progenitors in solar source regions. Our parametric survey suggests that the projection shape, cross-section radius, and toroidal flux of source flux ropes are crucial parameters in predicting magnetic structures and the propagation speed of CMEs, providing valuable insights for space weather prediction. On the one hand, the conclusion drawn here could be instructive in identifying the high-risk eruptions with the potential to induce stronger geomagnetic effects (B_z and propagation speed). On the other hand, our findings hold practical significance for refining the parameter settings of launched CMEs at 21.5 $R_\odot$ in heliospheric simulations, such as with EUHFORIA, based on observations for their progenitors in solar source regions.

Key words. magnetohydrodynamics (MHD) – methods: numerical – Sun: corona – Sun: coronal mass ejections (CMEs) – Sun: magnetic fields

1. Introduction

Coronal mass ejections (CMEs) represent the most intense and powerful explosions in the Solar System and are understood to be the primary drivers of changes in the solar-terrestrial space environment (Zhang et al. 2007; Chen 2011; Richardson & Cane 2012; Schmieder et al. 2015; Kilpua et al. 2017). When they reach the Earth, their southward magnetic fields can induce magnetic reconnection with the intrinsic geomagnetic field, thereby injecting energy and energetic particles from the solar wind into the magnetosphere. This has the potential to jeopardize satellites and even poses risks to human health (Gosling et al. 1987; Schrijver et al. 2015). Hence, predicting the properties of CMEs, particularly the magnetic structures (such as the B_z profile) and propagation speed before their full development, remains a priority for the field of space weather prediction.

Extensive observations have revealed that the core magnetic structure of CMEs is a magnetic flux rope, that is, bundles of twisted field lines winding around a common axis (Schmieder 2006; Cheng et al. 2017; Patsourakos et al. 2020; Liu 2020). White-light coronagraph observations have suggested that at

⋆ Corresponding authors; Stefaan.Poedts@kuleuven.be, chenpf@nju.edu.cn

least 40% of CMEs may incorporate a flux rope (Vourlidas et al. 2013), which is manifested as a dark cavity or bright core in observations (Chen 2011; Song et al. 2022). Furthermore, in situ detections of their consequences in interplanetary space, such as magnetic clouds, indicate that they often exhibit smooth and large-angle rotations in vector magnetic fields, suggesting the presence of helical field lines (Burlaga et al. 1981; Klein & Burlaga 1982).

Although the consensus regarding flux ropes as the magnetic cores of CMEs has been well accepted, the magnetic configuration of their progenitors remains elusive, so it is unclear as to whether a magnetic flux rope exists before the eruption or forms during it. Addressing this issue requires investigations into the magnetic structure of CME progenitors, such as hot channels (Zhang et al. 2012; Cheng et al. 2017), filaments (Schmieder et al. 2013; Chen et al. 2020), and cavities (Gibson 2015). For example, by diagnosing the magnetic configuration of eruptive filaments, Ouyang et al. (2015) demonstrated that flux ropes are not a necessary condition for CME progenitors. Similarly, Song et al. (2014) and Wang et al. (2017) found that flux ropes can form via magnetic reconnection during CME propagation but not before. Nonetheless, various observations and numerical modeling studies have demonstrated that flux ropes exist before the eruption in many events. For instance, certain observed proxies before the flare onset, such as conjugate coronal dimmings (Webb et al. 2000; Qiu et al. 2007; Wang et al. 2019, 2023; Xing et al. 2020a) and the sunspot scar (Xing et al. 2024), have been identified as the footpoints of preeruptive flux ropes. Additionally, numerous non-linear-force-free-field (NLFFF) extrapolations and data-driven MHD simulations of coronal magnetic fields have also indicated the existence of preexisting flux ropes (Cheung & DeRosa 2012; Guo et al. 2010, 2019, 2021, 2023, 2024a; Jiang et al. 2018; James et al. 2018; Duan et al. 2019; Kilpua et al. 2019; Inoue & Bamba 2021). Beyond case studies, the percentage of different preeruptive magnetic structures of CME progenitors has been quantified. Ouyang et al. (2017) investigated the magnetic configuration of 576 eruptive filaments and found that approximately 89% of them are supported by flux ropes. Wang et al. (2023) found that nine events display preeruptive coronal dimmings within a dataset of 28 CME events associated with dimmings. This implies that, even though it is not necessary, many CMEs result from the eruption of magnetic flux ropes.

In addition, numerous studies have demonstrated the feasibility of deducing the properties of CMEs in the outer corona and interplanetary space from their solar progenitors. For example, many works have revealed the consistency of the magnetic structure, such as the magnetic-field orientation and chirality, between interplanetary magnetic clouds and their progenitor filaments (Bothmer & Schwenn 1994; Marubashi 1997; Yurchyshyn et al. 2001; Wang et al. 2006; Rodriguez et al. 2008). In these cases, CME flux ropes largely maintain their initial orientation throughout the propagation process. However, there also exist CME flux ropes that undergo significant rotation in the eruption process, with the rotation direction strongly dependent on their projection shapes (Green et al. 2007; Zhou et al. 2020, 2022). Besides, a substantial amount of magnetic helicity carried by interplanetary magnetic clouds is inherited from their precursors in solar source regions. Xing et al. (2020a) discovered that toroidal fluxes, which are contributed by preexisting flux ropes to magnetic clouds, lie in a range of 40% to 88%. Through a comparison between the NLFFF extrapolation and reconstruction with in situ measurement of a magnetic cloud, Thalmann et al. (2023) found that the toroidal flux of the twisted magnetic structure in the solar source region can contribute 50% of that of its consequent magnetic cloud. These findings unveil the intrinsic linkages between preexisting flux ropes and their consequent CMEs, indicating the possibility of predicting magnetic structures and dynamics of CMEs from remote sensing observations in solar source regions, even prior to the onset of eruptions.

The main objective of this paper is to build a bridge between source magnetic flux ropes and their consequent CMEs. To this end, we constructed a series of flux ropes with different morphologies, sizes, and toroidal fluxes (intensity of the electric current). Subsequently, we simulated the self-consistent propagation processes of these flux ropes from the solar surface to 25 $R_\odot$ using a three-dimensional global coronal model called COolfluid COroNal UnsTructured (COCONUT; Perri et al. 2022), as realized in Linan et al. (2023) and Guo et al. (2024b). This paper is organized as follows. We describe the methodology in Section 2, exhibit the results in Section 3, and follow with a discussion in Section 4. Finally, we summarize the findings in Section 5.

2. Methodology

2.1. Reconstruction of preexisting magnetic flux ropes

To assess the impact of preexisting flux ropes in solar source regions on their consequent CMEs, it is crucial to construct flux ropes with high flexibility. For example, when investigating the influence of flux-rope morphology, it is advisable to allow the axes of flux ropes to be arbitrary rather than fixed. Moreover, the presence of conjugate coronal dimmings in observations suggests that eruptive flux ropes should be anchored to the solar surface rather than fully detached from it (Wang et al. 2017, 2023; Aulanier & Dudík 2019; Xing et al. 2020b). Given these observational constraints, Titov et al. (2018) proposed a novel method to construct magnetic fields including a thin flux rope, called Regularized Biot-Savart Laws (RBSL). This method can construct a force-free flux rope with an axis following an arbitrary path, facilitating the investigation of the morphology of flux ropes. Recently, Guo et al. (2024b) has implemented this technique in COCONUT and demonstrated its efficiency in modeling the initiation and propagation of a CME resulting from a sigmoid. Here, we explore the impacts of the parameters associated with the RBSL flux rope, particularly its morphology and toroidal flux, on the consequent CMEs using COCONUT.

The reconstruction of RBSL flux ropes involves four primary parameters: the axis path (C), cross-section radius (a), toroidal flux (F), and electric current (I). Among these, the axis path and cross-section radius jointly determine the geometry of a flux rope; the former controls its projection shape (S-, Z- or toroid-shaped), while the latter governs its overall size (slender or fat). The toroidal flux F influences both the magnetic-field strength and the electric current flowing through the flux rope ($F = \pm(3\mu_0 Ia)/5\sqrt{2}$, deduced from the equilibrium condition in the RBSL regime). To precisely control the flux rope morphology, similar to Guo et al. (2024b), the path of its axis is described by a theoretical curve that is defined as follows:

$$f(s) = \begin{cases} \frac{s(2x_c - s)}{x_c^2}\theta, & 0 \le s \le x_c \\ \frac{(s-2x_c+1)(1-s)}{(1-x_c)^2}\theta, & x_c < s \le 1 \end{cases} \quad (1)$$

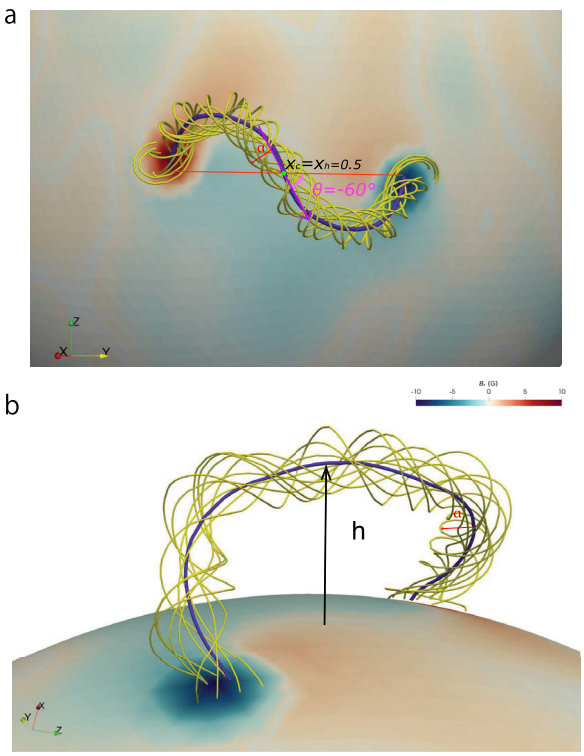

Fig. 1. Sketch of a typical Z-shaped magnetic flux rope with marked parameters of the RBSL flux rope. The purple and yellow tubes represent the flux-rope axis and twisted field lines, respectively.

$$x = (s - x_c)\cos f + x_c, \tag{2}$$
$$y = (s - x_c)\sin f, \tag{3}$$

$$z(x) = \begin{cases} \frac{x(2x_h - x)}{x_h^2} h, & 0 \le x \le x_h \\ \frac{(x - 2x_h + 1)(1 - x)}{(1 - x_h)^2} h, & x_h < x \le 1 \end{cases}, \tag{4}$$

where θ determines the projection angle with respect to the line connecting two footpoints, x_c controls the position where the projected curve intersects the line connecting two footpoints (referred to as the crossing point), x_h represents the apex position, and h indicates the apex height. We note that the sign of θ determines the projection shape (sign of non-local writhe) of the flux rope. Flux ropes that are constructed with values of $\theta > 0$, $\theta < 0$, and $\theta = 0$ correspond to S-shaped, Z-shaped and toroid-shaped morphologies, respectively. Figure 1 illustrates the configuration of the RBSL flux rope ($\theta = -60°$) with the key parameters marked, corresponding to a Z-shaped sigmoid.

In our parametric survey, flux ropes are positioned at the solar equator with fixed values of $x_c = x_h = 0.5$ and an apex height of $h = 120$ Mm. The parameters of our modeled flux ropes are in accordance with large-scale quiescent filaments in observations (Tandberg-Hanssen 1995). Figure 2 displays the flux ropes constructed with θ values of 60° (Figures 2a and 2b), 0° (Figures 2c and 2d), and −60° (Figures 2e and 2f), representing S-shaped, toroid-shaped, and Z-shaped morphologies, respectively. More details of the implementation process of the RBSL flux rope model in COCONUT can be found in Guo et al. (2024b).

2.2. Modeling the propagation of CME flux ropes with COCONUT

Once the flux rope was constructed, its subsequent eruption and propagation processes were simulated by COCONUT, a numerical model built on the Computational Object-Oriented Libraries for Fluid Dynamics (COOLFluiD) platform (Kimpe et al. 2005; Lani et al. 2005, 2013, 2014) and employing a fully implicit finite volume method to solve full 3D MHD equations on unstructured grids. The adoption of the implicit scheme and unstructured grids facilitates the rapid convergence of steady-state solutions within a domain that encompasses the entire global corona, also including the two poles. Consistent with our previous works (Linan et al. 2023; Guo et al. 2024b), we adopted a polytropic model to simulate the propagation of the CME flux rope from the solar surface to a distance of 25 $R_\odot$. This model takes into account a reduced adiabatic index γ of 1.05, emulating quasi-isothermal heating with limited energy injection (Mikić et al. 1999; Perri et al. 2022), which has demonstrated efficiency in reproducing the large-scale coronal magnetic fields and the propagation of CMEs with COCONUT (Perri et al. 2022; Kuźma et al. 2023; Linan et al. 2023). Despite the simplified thermodynamics tackled with this model, the evolution of the magnetic configuration remains relatively realistic.

The performance of the COCONUT model involves three main steps. First, we constructed the background solar wind using the time-independent relaxation module for the steady-state solution of the background solar wind (Perri et al. 2022). In this work, the background large-scale magnetic fields and the solar wind are based on the solar magnetogram ("hmi.Synoptic_Mr_720s_small") from 2019 July 2 provided by the Helioseismic and Magnetic Imager (HMI; Scherrer et al. 2012) on board the Solar Dynamics Observatory (SDO; Pesnell et al. 2012) for two reasons. On the one hand, this data corresponds to the minimum of solar activity, thereby minimizing the impacts of the background solar wind on CME propagation while still providing a relatively realistic coronal magnetic field environment compared to the dipole configuration. On the other hand, the simple magnetic configuration in the solar minimum activity enhances the stability of the convergence process. In particular, we do not use the raw HMI magnetogram directly as the inner boundary. Instead, the original map is processed using the spherical harmonic projection with a maximum reconstruction frequency of $l_{\max} = 20$. This preprocessing reduces the strength of the magnetic field, corrects some null values, and smooths small-scale structures. For more details on the preprocessing of input magnetograms, we refer to Kuźma et al. (2023) and Perri et al. (2023). Additionally, the solar wind configuration that has been reconstructed from this data has undergone extensive examination in our previous COCONUT papers (Kuźma et al. 2023; Linan et al. 2023). Next, we superposed the constructed flux ropes into the relaxed solar wind to propel CMEs. Finally, we switched the steady-state relaxation run to a time-dependent simulation in order to study the eruption and propagation process of CMEs. It should also be noted that our flux ropes are inserted into the solar quiet regions (see Figure 2), which means that our simulation results mainly concentrate on the CMEs erupting from quiescent filaments. Linan et al. (2023) and Guo et al. (2024b) provided more details about the CME module in COCONUT.

Our simulation encompasses the entire global corona, including both poles, where r spans from the solar surface to a distance of 25 $R_\odot$ in radius, ϕ ranges from −180° to 180° in longitude, and θ ranges from −90° to 90° in latitude. The

Table 1. Parameters and results in different cases.

	Case	θ	F	a	$V_{\rm CME}$
		(°)	($\times 10^{20}$ Mx)	(Mm)	(km s^{-1})
S	S1	60	3	35	465
	S2	60	12	105	467
	S3	60	24	105	697
Z	Z1	−60	3	35	504
	Z2	−60	12	105	456
	Z3	−60	24	105	708
Toroid	T1	0	3	35	484
	T2	0	12	105	445
	T3	0	24	105	702
	T4	0	3	105	–

Notes. The arguments of θ, F, a, and $V_{\rm CME}$ denote the writhe angle, toroidal flux, cross-section radius of the flux rope, and the propagation speed of its consequent CME, respectively.

computational domain is discretized with a six-level subdivision of a geodesic polyhedron, resulting in approximately 1.5 million cells (see Brchnelova et al. 2022a for more details). The boundary conditions are prescribed using the approach described in Linan et al. (2023) and Guo et al. (2024b). Specifically, at the inner boundary, the radial magnetic field is constrained by the observed magnetogram, while other magnetic field components are determined by zero-gradient extrapolation. The pressure and density are fixed at values of $p_\odot = 4.15 \times 10^{-2}$ dyn cm^{-2} and $\rho_\odot = 1.67 \times 10^{-16}$ g cm^{-3}, respectively. The atmosphere of our model is set from the solar corona, and the effects of the photosphere, chromosphere and transition region on the solar wind and CME propagation are omitted. To eliminate spurious electric fields near the solar surface, the velocity direction is prescribed along magnetic field lines (Brchnelova et al. 2022b). The outer boundary relies upon a zero-gradient extrapolation under the assumption of a super-fast outflow.

2.3. Dataset for parametric survey

The input parameters for the implemented flux ropes are summarized in Table 1. Cases labeled with "S", "Z", and "T" symbols represent flux ropes with S-shaped, Z-shaped, and toroid-shaped projection shapes, respectively. The variation in the projection shape is achieved by changing the value of θ. Cases labeled with "1", "2", and "3" subscripts correspond to the benchmark, cases with a large cross-section radius, and cases with larger toroidal fluxes, respectively. It is worth noting that increasing the cross-section radius of the flux rope inadvertently decrease its magnetic-field strength if keeping the toroidal flux constant. In order to compensate for the magnetic field strength change resulting from the cross-section radius change, we employed a strategy of simultaneously increasing both the cross-section radius and toroidal flux in cases S2, T2, and Z2.

Figure 2 displays the reconstructed flux ropes with different projection shapes. The panels, from top to bottom, show S-shaped, toroid-shaped, and Z-shaped flux ropes, respectively. The left and right panels depict slender (small cross-section radius) and fat (large cross-section radius) flux ropes, respectively. It is evident that slender flux ropes are more twisted compared to fat ones, which is consistent with previous results showing that the twist number of a flux rope increases with its aspect ratio (Wang et al. 2016; Guo et al. 2021). In particular, filaments with a positive helicity typically exhibit S-shaped morphology. Despite this, certain cases may deviate from this empirical rule (Zhou et al. 2020), suggesting that the "Z" cases in our dataset are also plausible.

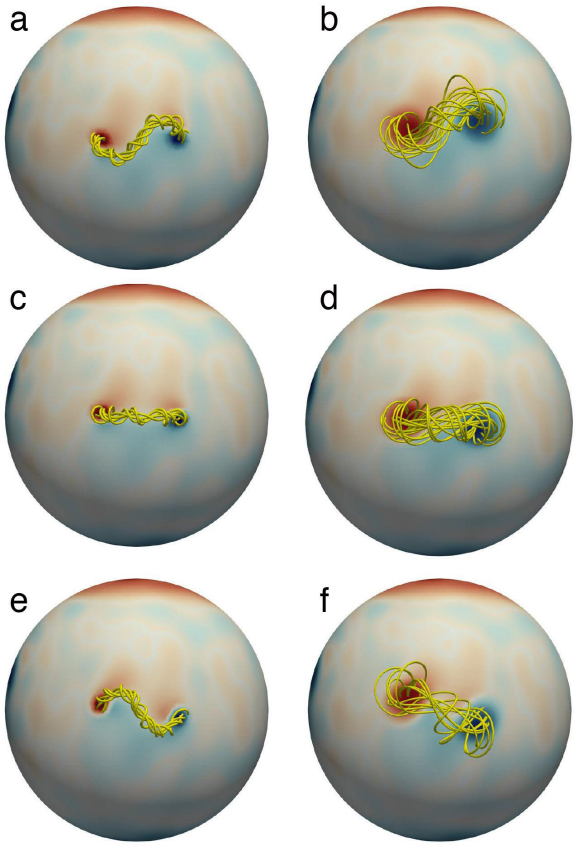

Fig. 2. Magnetic structures of flux ropes in typical cases. Panels a–f show the cases of S1, S2, T1, T2, Z1, and Z2, respectively. The yellow lines represent flux ropes, which are traced from the flux rope footpoints. The left and right panels depict flux ropes with the small and large cross-section radius, respectively.

The effects of the preexisting flux ropes on their ensuing CMEs can be elucidated through comparative studies. For example, comparing cases labeled "S", "Z", and "T" allows us to understand the influence of the projection shape of flux ropes. The comparison between cases denoted by "1" and "2" subscripts enables us to assess the effect of the cross-section radius, while comparing cases labeled with "2" and "3" subscripts illustrates how the toroidal flux of flux ropes influences their eruption and propagation processes. This paper mainly concentrates on the propagation and large-scale magnetic structures of CMEs in the outer corona rather than their initiation processes. The inserted flux ropes are in non-equilibrium and are torus-unstable. As a result, CME flux ropes will directly erupt and be accelerated to a high speed upon insertion.

3. Numerical results

3.1. Impacts on magnetic structure and propagation speed of coronal mass ejections

First, we investigated how the morphology of the preexisting flux ropes influences the magnetic structures of their resulting CMEs. Figures 3 and 4 present typical field lines of CME flux ropes 3.2 h after the eruption, traced from the footpoints of the flux rope. It can be seen that CMEs retain certain features of

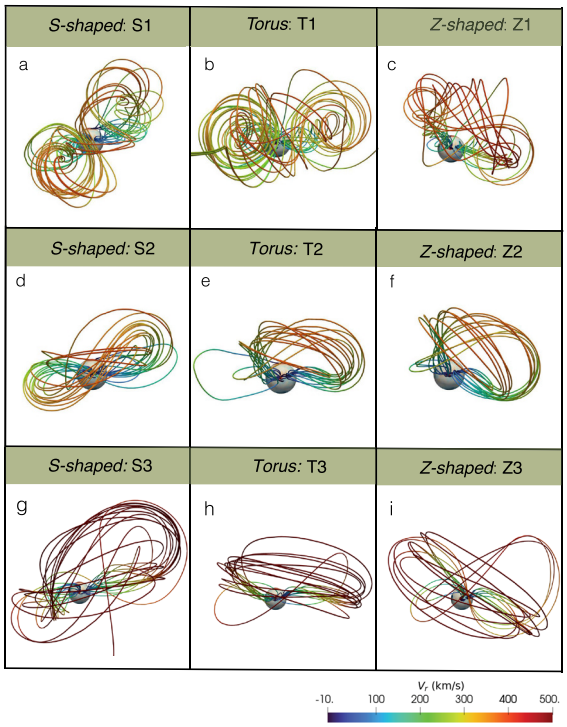

Fig. 3. Top views of CME magnetic structures at 3.2 h. The field lines are traced from the locations of the flux-rope footpoints at the beginning. The color represents the radial velocity, which ranges from −10 to 500 km/s.

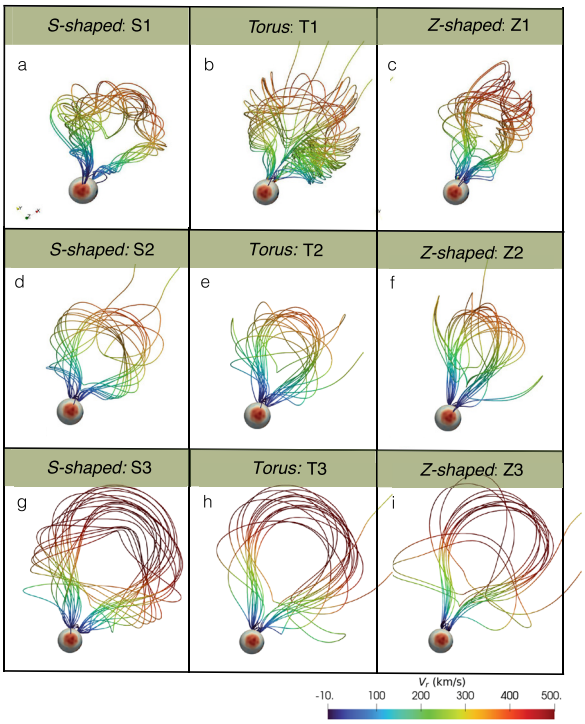

Fig. 4. Same as Figure 3 but for the side view.

their progenitors in many senses, even though they have propagated to a distance far beyond 10 $R_\odot$. For example, CME flux ropes inherit their initial morphology to a great extent, maintaining the sigmoid (Figure 3a), toroid (Figure 3b), and reversed sigmoid (Figure 3c). On top of that, the size or thickness of the preexisting flux ropes is crucial in determining the twist properties of CME flux ropes. The CMEs originating from slender flux ropes are more twisted than those erupting from fat ones, which is consistent with the findings for CME progenitors (Guo et al. 2021) and CME consequences in interplanetary space (Wang et al. 2016). Moreover, it seems that the bulk-up of initial flux ropes can mitigate the impacts of the projection shape on CME structures. To sum up, our results strongly indicate that both the projection shape and thickness of source flux ropes are worthy of consideration when predicting the magnetic structures of CMEs in the outer corona.

In the following, we explore the impacts of the morphology and toroidal flux of flux ropes on the thermodynamics of their resulting CMEs. Figures 5 and 6 illustrate the temperature and radial velocity distribution on the equatorial plane, respectively, from which one can see that CMEs are nearly outlined by the heated areas, driving forward high-speed flows. Furthermore, it can be seen that an increase in the toroidal flux of source flux ropes results in faster and hotter CMEs. However, the variation due to the thickness (cross-section radius) of source flux ropes is relatively smaller. In particular, we found that the CME temperature is smaller when simultaneously increasing the toroidal flux and expanding the cross-section radius of flux ropes (by comparing cases T1/T2, S1/S2, and Z1/Z2). This is due to the decrease in electric current density when increasing the volume of the flux rope bulk. Of special note is that the hot and upward flows below flux ropes predicted in the stand flare model (Carmichael 1964; Sturrock 1966; Hirayama 1974; Kopp & Pneuman 1976) can be identified, especially in cases S3, T3, and Z3, which is generally regarded as the result of magnetic reconnection. Therefore, magnetic reconnection could be more pronounced in CMEs erupting from flux ropes with high toroidal fluxes over the same propagation duration.

To quantify the propagation speed of CMEs, we made time-distance diagrams, shown in Figure 7, by tracking the CME leading edges measured from the radial direction of the eruption. As a result, the propagation speed of CMEs can be estimated through linear fitting. We found that CMEs erupting from flux ropes with a large toroidal flux (Cases S3, Z3, and T3) propagate faster compared to the other cases. However, the impact of its projection shape is not apparent. This suggests that an effective approach to propel fast CMEs would be to increase the toroidal flux of source flux ropes, which is consistent with the results of Linan et al. (2023).

3.2. Impacts on in situ detection of magnetic clouds

In this subsection, we delve into an exploration of how source flux ropes influence the in situ plasma profiles of their resulting CMEs. In situ measurements provide greater precision in diagnosing the local characteristics of CME plasma when compared to remote sensing observations. To this end, we placed two virtual spacecraft at a heliocentric distance of 21.5 $R_\odot$ and designed to pass roughly through the nose and flank of the modeled CMEs, where satellite A passes through the CME nose and satellite B mainly detects the features of the CME flank, as shown in Figure 8. It is noteworthy that the distance of 21.5 $R_\odot$ serves as the inner boundary of our heliosphere MHD model, EUHFORIA (Pomoell & Poedts 2018; Poedts et al. 2020). Figures 9 and 10 illustrate the detected plasma profiles in terms of speed, vector magnetic fields, density, and temperature at satellites A and B, respectively.

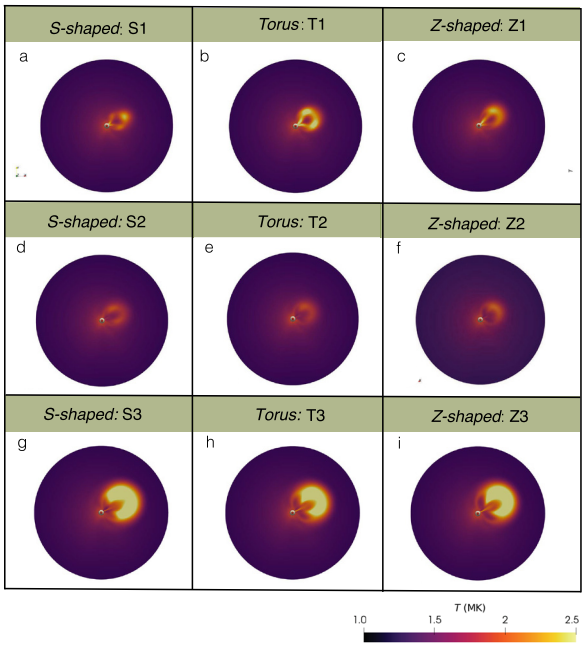

Fig. 5. Temperature distributions on the equatorial plane at 3.2 h.

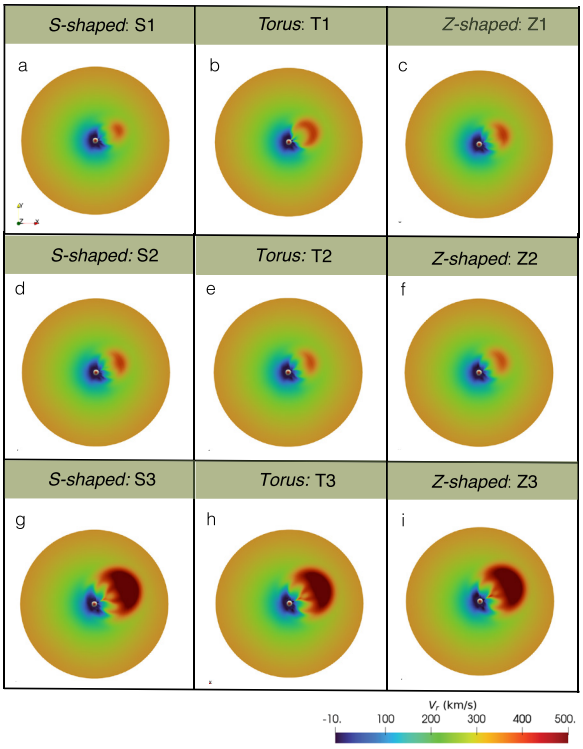

Fig. 6. Radial velocity distributions on the equatorial plane at 3.2 h.

Figure 9a presents the in situ profiles of cases S1, T1, and Z1 measured at satellite A (CME nose), in which the detected CMEs result from the eruption of slender flux ropes. It can be well seen that the projection shape of source flux ropes leads to a significant change in the plasma profiles of CMEs, especially for magnetic fields. For instance, the CMEs resulting from the eruptions of Z-shaped and toroid-shaped flux ropes exhibit a stronger magnetic-field amplitude compared to the S-shaped case. This may be due to the enhanced magnetic reconnection between S-shaped CME flux ropes and overlying magnetic fields, as suggested by the magnetic connectivity in Figure 2. Additionally, the Z-shaped case shows a larger negative B_z component than the S-shaped case, which is attributed to the fact that, in principle, Z-shaped flux ropes with positive magnetic helicity can carry stronger negative B_z magnetic fields, as shown in Figure 2.

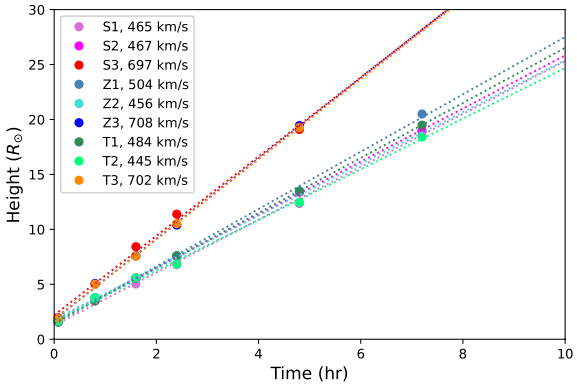

Fig. 7. Time-distance diagram of CMEs. The dotted lines are fitted with a linear trend.

Regarding the velocity profiles, despite the similarity in the arrival time of these CMEs, their profiles have an obvious difference. We observed a late-phase in case T1 (red line), which is characterized by heating and acceleration. Similar phenomena were also found in observations from radio occultation measurements with the Akatsuki spacecraft (Ando et al. 2015). This could be explained by the magnetic reconnection taking place below the flux rope, consistent with the results in Figure 4, where the highly curved field lines and underlying flare loops serve as evidence of magnetic reconnection (Guo et al. 2024b). It is worth noting that the late phase is not significantly visible in the toroid-shaped flux ropes with large cross-section radii (cases T2 and T3), which may be due to the different dominant reconnection geometries in these cases. Although the flux ropes in cases T1, T2, and T3 are similar in geometry, they differ significantly in twist number, with the slender flux rope in case T1 being more twisted than the fat ones in cases T2 and T3. As a result, separatrices are more likely to exist between CME flux ropes and ambient arcades in case T1, enhancing the interchange magnetic reconnection that flux ropes may participate in. Additionally, the flux ropes with a large cross-section radius occupy a portion of volume originally belonging to the overlying background magnetic fields, thereby reducing the likelihood of magnetic reconnection in the overlying arcade field lines. Instead, the reconnection between two flux-rope legs could be more dominant. This may result in the late phase being less visible in cases T2 and T3 compared to case T1.

Nevertheless, the influences from the morphology are highly sensitive to the cross-section radius of the flux rope. As depicted in Figure 9b, the in situ profiles of CMEs that are initiated from fat flux ropes exhibit greater similarity, regardless of the various projection shapes of the preexisting flux ropes. Hence, our results suggest that the axis path of the preexisting flux ropes becomes less critical in modeling the propagation of their resulting CMEs when the cross-section radius is large enough. In this scenario, the flux-rope model with a simply straight toroidal shape remains sufficiently accurate in simulating the propagation of CMEs, even though observed flux-rope proxies, such as filaments, follow intricate paths. Figure 9c displays cases with high toroidal fluxes (S3, T3, Z3). In comparison to the results in Figure 9b, flux ropes with high toroidal fluxes can propel CMEs at higher speeds.

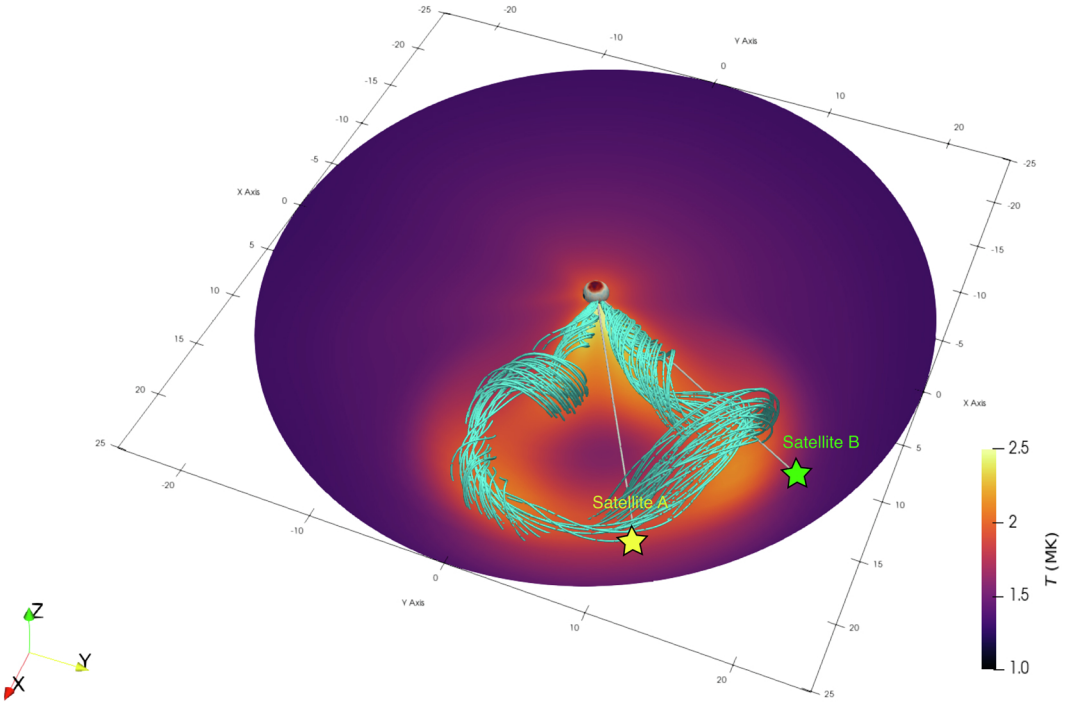

Fig. 8. Positions of two virtual satellites that are used to detect CMEs. Satellites A and B pass through the nose and flank of modeled CMEs, respectively.

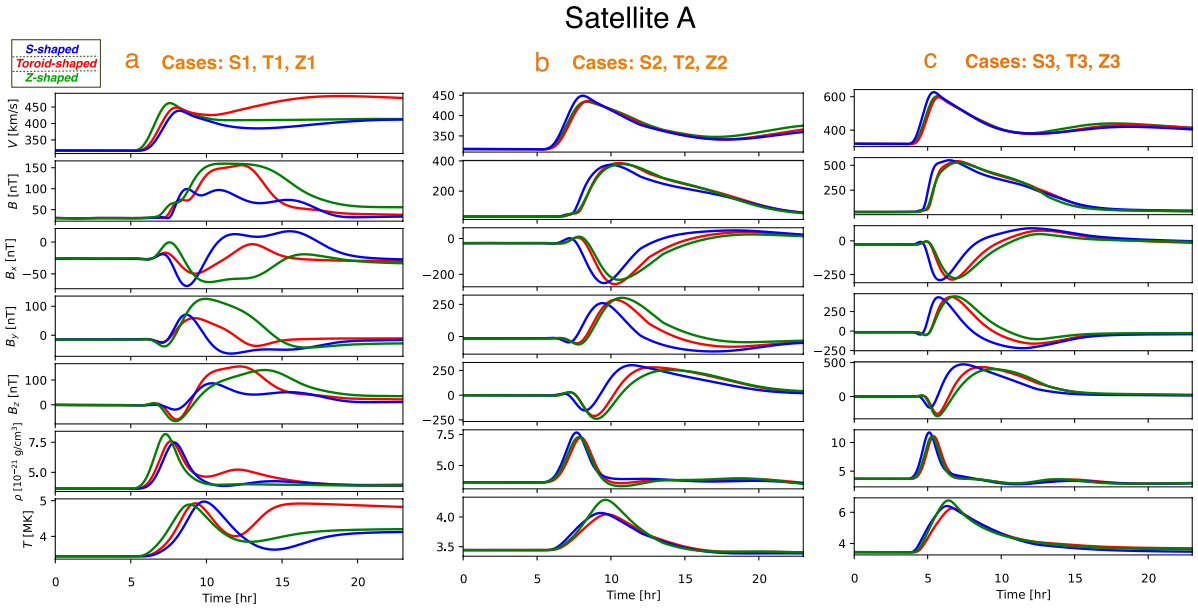

Fig. 9. In situ plasma profiles measured at satellite A. Panels a, b, and c present the cases with "1", "2", and "3" subscripts, respectively. The blue, red, and green lines represent the S-shaped, toroid-shaped, and Z-shaped cases, respectively.

The above detection primarily reflects the plasma characteristics of the CME nose. To understand the results of the CME flank, we present the in situ plasma profiles detected by satellite B in Figure 10. Similar to the results measured from the CME nose, the in situ profiles of CMEs initiated from fat flux ropes still remain similar to a large extent, even when detected at their flanks. Moreover, the differences in profiles resulting from the morphology of the source flux ropes are more pronounced at the CME flanks. This may be due to the fact that the non-radial motions (e.g., the rotation direction) differ significantly depending on the projection morphology of the source flux ropes (Zhou et al. 2020); for example, S-shaped flux ropes generally rotate clockwise.

4. Discussions

4.1. Impacts of the morphology of source magnetic flux ropes on their consequent coronal mass ejections

Although magnetic flux ropes detected in the interplanetary space are often modeled as simple cylindrical twisted flux tubes anchored to the solar surface (Isavnin 2016), it is

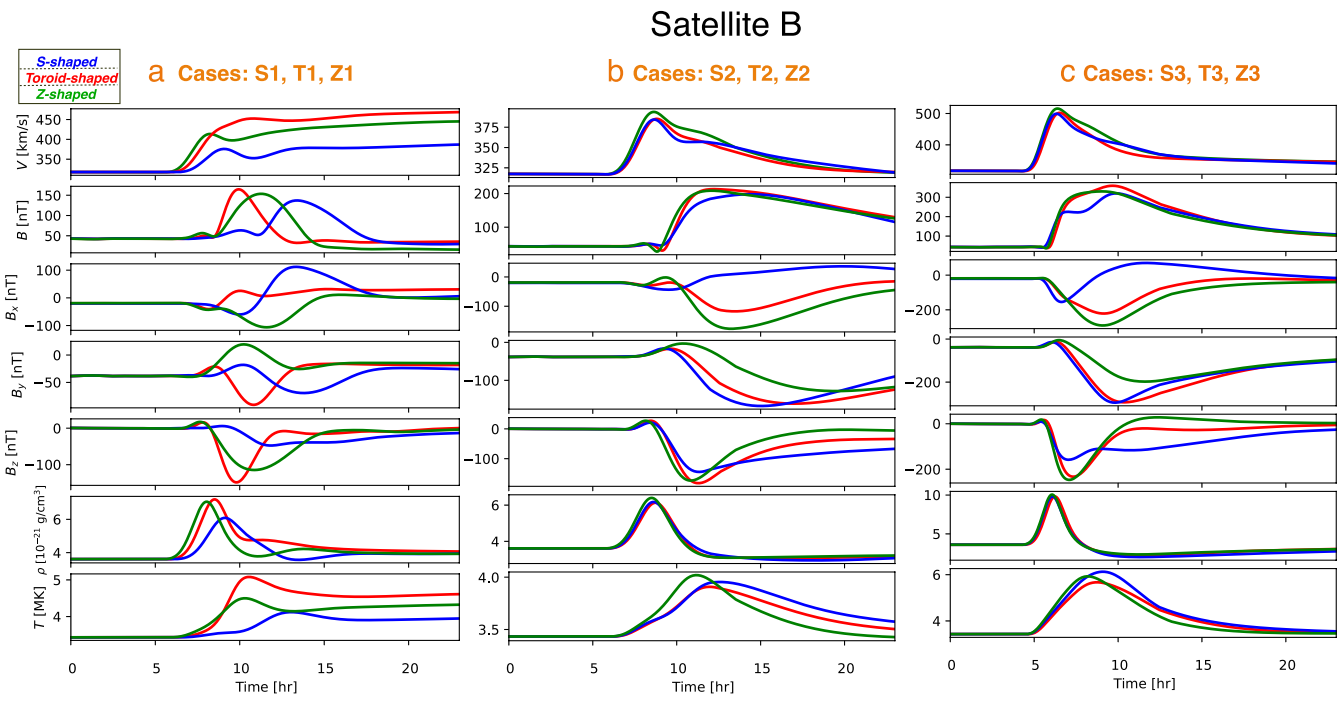

Fig. 10. In situ plasma profiles measured at satellite B.

widely accepted that their progenitors in solar source regions, which are conventionally proxied by sigmoids, hot channels, coronal cavities, and filaments, often exhibit a complicated and irregular morphology. For instance, sigmoids and hot channels typically display S-shaped or Z-shaped structures (Cheng et al. 2017). Furthermore, prominences often show significant variations in morphology, appearing as clouds, stems, horns, flames, and plumes. Their length can vary considerably depending on their magnetic surroundings, ranging from less than 100 Mm in active regions to up to 600 Mm in quiet regions (Tandberg-Hanssen & Malville 1974; Filippov & Den 2000; Mackay et al. 2010; Chen et al. 2020; Gunár et al. 2023). Additionally, the width of quiescent filaments is notably larger compared to active-region types, suggesting potential differences in the cross-section radius of their supporting magnetic flux ropes (Guo et al. 2022).

Despite the intricate shapes exhibited by these CME progenitors in observations, the majority of numerical models extensively simplify them with regular and simple shapes, such as the spheromark (Kataoka et al. 2009; Shiota et al. 2010; Verbeke et al. 2019), toroid (Titov et al. 2014; Linan et al. 2023), and teardrop (Gibson & Low 1998; Jin et al. 2017). The impact of deviations in modeled flux ropes from observations in the solar source region on the magnetic structures of their resulting CMEs needs to be examined. Additionally, it is important to identify the conditions under which the source flux rope can be simplified to a simple and regular morphology, such as a toroid.

Our simulation results unveil the impact of source flux rope morphology on the resulting CMEs. As depicted in the top panels of Figures 4 and 9a, the CMEs erupting from flux ropes with different projection shapes exhibit distinct magnetic structures and in situ plasma profiles. Specifically, the CME originating from an S-shaped flux rope displays a weaker negative B_z component compared to the Z- and toroid-shaped cases. If CME flux ropes maintain the same orientation in the subsequent propagation process, the stronger geomagnetic effects could be induced in latter cases. However, as the cross-section radius of the flux rope increases, the influences from the flux-rope morphology become less pronounced, as evidenced in Figures 9b and 9c. This suggests that simplifying a flux rope path with a simple shape to model the propagation of CMEs is reliable when its cross-section radius is sufficiently large. Guo et al. (2022) revealed a spatial relationship between filament materials and their supporting flux ropes based on pseudo-3D simulations for the filament formation: filament materials occupy almost a quarter of the flux rope. Based on this and the parameter survey in this paper, we suggest that the morphology of flux ropes becomes less important when the ratio between the width and length of their hosting filaments exceeds 0.125. Conversely, it becomes essential to measure the realistic paths of flux ropes from their observed proxies. Our findings strongly underscore the advantage of the RBSL method, as it is capable of precisely modeling a flux rope with an axis of arbitrary shape.

On the other hand, the above results reveal the importance of considering the cross-section radius of the flux rope in future CME prediction tools. Various approaches can be employed to derive these topology parameters. The first method relies on the 3D reconstruction of coronal magnetic fields, such as the NLFFF extrapolation (Guo et al. 2016, 2019, 2021) and data-driven models (Cheung & DeRosa 2012; Jiang et al. 2016; Pomoell & Poedts 2018; Guo et al. 2024a), which can directly construct magnetic flux ropes and thus outline key topology parameters. The second involves utilizing observational features to trace flux ropes, such as the filament width, drainage sites, flare ribbons, dimming, and sunspot scar (Harra & Sterling 2001; Wang et al. 2017, 2023; Aulanier & Dudík 2019; Xing et al. 2020a, 2024). Therefore, to enhance the accuracy in CME prediction, it is important and urgent to develop novel approaches to diagnose the key topology parameters of source magnetic flux ropes, such as the axis path and cross-section radius. However, it should be noted that, the flux ropes in our dataset are positive in helicity sign and positioned at the solar equator. This implies that the results in

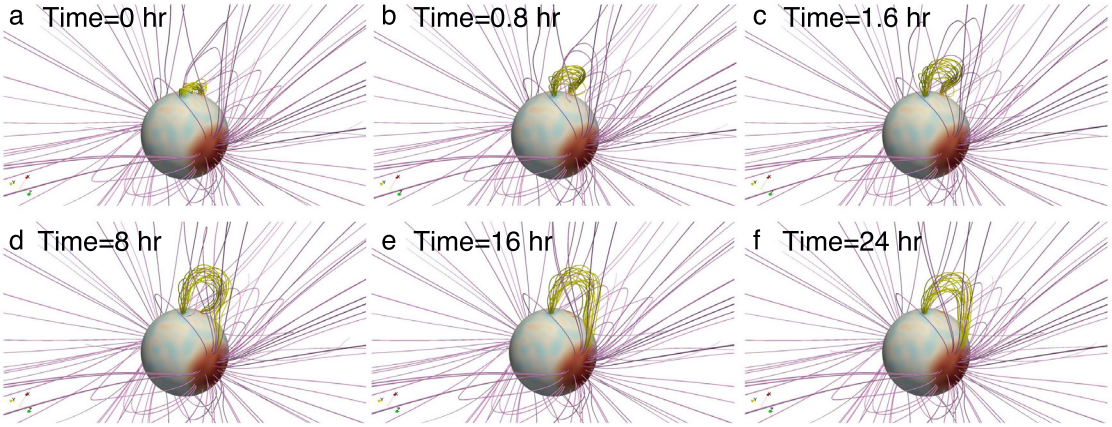

Fig. 11. Evolution of magnetic fields of a confined eruption (case T4). The yellow and pink lines represent the flux rope and the background solar-wind magnetic fields, respectively.

real observations may be more complicated than the conclusions drawn in this paper.

4.2. Linking the coronal mass ejection propagation speed and successfulness with its progenitor

It is widely accepted that the speeds of CMEs and their associated driven shocks are closely linked to particle acceleration and the induced geomagnetic effects (Chen 2011; Webb & Howard 2012; Tsurutani et al. 2023). Therefore, identifying flux-rope parameters that are sensitive to CME speed is crucial for forecasting the impacts of CMEs on the heliospheric environment.

As shown in Figure 7, the propagation speed of CMEs is not sensitive to the morphology of their source flux ropes, but it significantly increases with the toroidal flux. Similar conclusions concerning the effects of toroidal flux have also been drawn in previous studies. For example, Qiu et al. (2007) found that CME speed increases with the reconnection fluxes identified from flare ribbons. Besides, Chen et al. (2006) found that the CME speed is roughly proportional to the average magnetic strength of the source photosphere. Su et al. (2011) found that an increase in toroidal flux can lead to the catastrophic loss of equilibrium, thereby resulting in an eruption. Zhang et al. (2020) found that flux feeding can cause the flux rope to rise. Additionally, global MHD simulations based on the Gibson-Low flux rope model (Jin et al. 2017) and Titov-Démoulin-modified model (TDm; Linan et al. 2023) have also revealed that CMEs erupting from flux ropes with a higher toroidal flux tend to propagate more rapidly. On the other hand, the source magnetic flux ropes in cases T1 and T4 have the same toroidal flux, but case T4 has a larger, different cross-section radius. The fact that case T4 turns out to be a confined eruption implies that the large size of the source flux rope may hinder the CME from erupting at a high speed (e.g., via a bigger drag force) and may even result in failed eruptions.

Given this insight, we can infer that the eruption may be constrained in the solar atmosphere when the toroidal flux of the source flux ropes is sufficiently small. Previous works have demonstrated that strong overlying magnetic fields can constrain solar eruptions (i.e., magnetic cage Amari et al. 2018). However, the properties of the core fields should also be effective at influencing the kinetics of the resulting CMEs. To investigate this, we conducted a simulation, which we called case T4, in which the toroidal flux is approximately one-eighth of that in case T2 while the other parameters remained constant. The 3D evolution of the magnetic fields in case T4 is illustrated in Figure 11. Initially, the flux rope undergoes a rapid ascent, accompanied by a slight clockwise rotation due to the release of twist. Following this, the rising of the flux rope starts to decelerate, with some twisted field lines turning into expanding loops. Meanwhile, it interacts with neighboring streamers that extend from the polar regions through interchange reconnection. As a result, after one day of evolution, the twisted flux rope disintegrates into the overlying loops, with one of their footpoints migrating toward the polar regions. This case demonstrates that the toroidal flux not only plays a crucial role in determining CME speed but that it can also determine the success or failure of an eruption. Therefore, our parametric survey suggests that deriving the toroidal flux of the preeruptive flux rope is significant in CME forecasting, as it enables prediction of a flux rope's ability to escape from the corona and the speed of the eruption.

5. Summary

In this paper, we have investigated the impacts of magnetic flux ropes in solar source regions on their resulting CMEs with the aid of 3D global MHD simulations from the solar surface to a distance of 25 $R_\odot$. Our parameter survey mainly focused on the CME events initiated from quiescent filament eruptions in observations. Our parametric survey established a bridge between the large-scale CMEs at 20 $R_\odot$ and their solar source regions, leading to the following conclusions:

1. The projection shape of the source flux ropes is considerable in changing the magnetic structures and in situ plasma profiles of their resulting CMEs, particularly for CMEs erupting from slender flux ropes. This underscores the importance of accurately measuring the morphology of flux ropes from CME progenitors in observations. However, the impact of the projection shape on the speed of CMEs is not significant.
2. The ratio of the cross-section radius/thickness of a source flux rope is a crucial parameter for CME prediction. We find that the effects arising from the projection shape of source flux ropes on their resulting CMEs can be ignored, as their cross-section radius is sufficiently large.
3. Under the same overlying magnetic fields, the propagation speed of CMEs increases with the toroidal flux of their source flux ropes. Additionally, we found that there is a tendency for confined eruptions to occur when the toroidal flux of the source flux rope is too small.

The outcomes of this paper offer valuable insights for space weather forecasting. First, they aid in identifying high-risk events with the potential to cause geomagnetic effects from their progenitors in solar source regions. Second, these findings can provide constraints for the input parameters of launched CMEs at 21.5 $R_\odot$ in heliospheric simulations, such as with EUHFORIA. Moreover, the bridge between CMEs and their source flux ropes, as revealed by our parametric survey, offers valuable insights for reproducing real eruption events in observations.

Acknowledgements. This work is supported by the National Key R&D Program of China (2020YFC2201200, 2022YFF0503004), NSFC (12127901, 12333009), Shanghai Institute of Satellite Engineering (SAST2021-046, D050101), projects C14/19/089 (C1 project Internal Funds KU Leuven), G.0B58.23N and G.0025.23N (WEAVE) (FWO-Vlaanderen), SIDC Data Exploitation (ESA Prodex-12), AFOSR FA9550-18-1-0093, and Belspo project B2/191/P1/SWiM. The resources and services used in this work were provided by the VSC (Flemish Supercomputer Centre), funded by the Research Foundation – Flanders (FWO) and the Flemish Government.

References

Amari, T., Canou, A., Aly, J.-J., Delyon, F., & Alauzet, F. 2018, Nature, 554, 211
Ando, H., Shiota, D., Imamura, T., et al. 2015, J. Geophys. Res.: Space Phys., 120, 5318
Aulanier, G., & Dudík, J. 2019, A&A, 621, A72
Bothmer, V., & Schwenn, R. 1994, Space Sci. Rev., 70, 215
Brchnelova, M., Zhang, F., Leitner, P., et al. 2022a, J. Plasma Phys., 88, 905880205
Brchnelova, M., Kuźma, B., Perri, B., Lani, A., & Poedts, S. 2022b, ApJS, 263, 18
Burlaga, L., Sittler, E., Mariani, F., & Schwenn, R. 1981, J. Geophys. Res., 86, 6673
Carmichael, H. 1964, NASA Spec. Publ., 50, 451
Chen, P. F. 2011, Liv. Rev. Sol. Phys., 8, 1
Chen, A. Q., Chen, P. F., & Fang, C. 2006, A&A, 456, 1153
Chen, P.-F., Xu, A.-A., & Ding, M.-D. 2020, Res. Astron. Astrophys., 20, 166
Cheng, X., Guo, Y., & Ding, M. 2017, Sci. China Earth Sci., 60, 1383
Cheung, M. C. M., & DeRosa, M. L. 2012, ApJ, 757, 147
Duan, A., Jiang, C., He, W., et al. 2019, ApJ, 884, 73
Filippov, B. P., & Den, O. G. 2000, Astron. Lett., 26, 322
Gibson, S. 2015, Astrophys. Space Sci. Lib., 415, 323
Gibson, S. E., & Low, B. C. 1998, ApJ, 493, 460
Gosling, J. T., Baker, D. N., Bame, S. J., et al. 1987, J. Geophys. Res., 92, 8519
Green, L. M., Kliem, B., Török, T., van Driel-Gesztelyi, L., & Attrill, G. D. R. 2007, Sol. Phys., 246, 365
Gunár, S., Labrosse, N., Luna, M., et al. 2023, Space Sci. Rev., 219, 33
Guo, Y., Schmieder, B., Démoulin, P., et al. 2010, ApJ, 714, 343
Guo, Y., Xia, C., Keppens, R., & Valori, G. 2016, ApJ, 828, 82
Guo, Y., Xu, Y., Ding, M. D., et al. 2019, ApJ, 884, L1
Guo, J. H., Ni, Y. W., Qiu, Y., et al. 2021, ApJ, 917, 81
Guo, J. H., Ni, Y. W., Zhou, Y. H., et al. 2022, A&A, 667, A89
Guo, J. H., Ni, Y. W., Zhong, Z., et al. 2023, ApJS, 266, 3
Guo, J. H., Ni, Y. W., Guo, Y., et al. 2024a, ApJ, 961, 140
Guo, J. H., Linan, L., Poedts, S., et al. 2024b, A&A, 683, A54
Harra, L. K., & Sterling, A. C. 2001, ApJ, 561, L215
Hirayama, T. 1974, Sol. Phys., 34, 323
Inoue, S., & Bamba, Y. 2021, ApJ, 914, 71
Isavnin, A. 2016, ApJ, 833, 267
James, A. W., Valori, G., Green, L. M., et al. 2018, ApJ, 855, L16
Jiang, C., Wu, S. T., Yurchyshyn, V., et al. 2016, ApJ, 828, 62
Jiang, C., Zou, P., Feng, X., et al. 2018, ApJ, 869, 13
Jin, M., Manchester, W. B., van der Holst, B., et al. 2017, ApJ, 834, 172
Kataoka, R., Ebisuzaki, T., & Kusano, K. 2009, J. Geophys. Res.: Space Phys., 114, A10102
Kilpua, E. K. J., Balogh, A., von Steiger, R., & Liu, Y. D. 2017, Space Sci. Rev., 212, 1271
Kilpua, E. K. J., Lugaz, N., Mays, M. L., & Temmer, M. 2019, Space Weather, 17, 498
Kimpe, D., Lani, A., Quintino, T., Poedts, S., Vandewalle, S., et al. 2005, Recent Advances in Parallel Virtual Machine and Message Passing Interface (Berlin, Heidelberg: Springer)
Klein, L. W., & Burlaga, L. F. 1982, J. Geophys. Res., 87, 613
Kopp, R. A., & Pneuman, G. W. 1976, Sol. Phys., 50, 85
Kuźma, B., Brchnelova, M., Perri, B., et al. 2023, ApJ, 942, 31
Lani, A., Quintino, T., & Kimpe, D. 2005, Computational Science - ICCS 2005 (Berlin, Heidelberg: Springer)
Lani, A., Villedieu, N., Bensassi, K., et al. 2013, AIAA 2013-2589, 21th AIAA666 CFD Conference, San Diego (CA) (Reston, VA : American Institute of Aeronautics and Astronautics)
Lani, A., Yalim, M. S., & Poedts, S. 2014, Comp. Phys. Commun., 185, 2538
Linan, L., Regnault, F., Perri, B., et al. 2023, A&A, 675, A101
Liu, R. 2020, Res. Astron. Astrophys., 20, 165
Mackay, D. H., Karpen, J. T., Ballester, J. L., Schmieder, B., & Aulanier, G. 2010, Space Sci. Rev., 151, 333
Marubashi, K. 1997, Geophys. Monogr. Ser., 99, 147
Mikić, Z., Linker, J. A., Schnack, D. D., Lionello, R., & Tarditi, A. 1999, Phys. Plasmas, 6, 2217
Ouyang, Y., Yang, K., & Chen, P. F. 2015, ApJ, 815, 72
Ouyang, Y., Zhou, Y. H., Chen, P. F., & Fang, C. 2017, ApJ, 835, 94
Patsourakos, S., Vourlidas, A., Török, T., et al. 2020, Space Sci. Rev., 216, 131
Perri, B., Leitner, P., Brchnelova, M., et al. 2022, ApJ, 936, 19
Perri, B., Kuźma, B., Brchnelova, M., et al. 2023, ApJ, 943, 124
Pesnell, W. D., Thompson, B. J., & Chamberlin, P. C. 2012, Sol. Phys., 275, 3
Poedts, S., Lani, A., Scolini, C., et al. 2020, J. Space Weather Space Clim., 10, 57
Pomoell, J., & Poedts, S. 2018, J. Space Weather Space Clim., 8, A35
Qiu, J., Hu, Q., Howard, T. A., & Yurchyshyn, V. B. 2007, ApJ, 659, 758
Richardson, I. G., & Cane, H. V. 2012, J. Space Weather Space Clim., 2, A02
Rodriguez, L., Zhukov, A. N., Dasso, S., et al. 2008, Geophys. Monogr. Ser., 26, 213
Scherrer, P. H., Schou, J., Bush, R. I., et al. 2012, Sol. Phys., 275, 207
Schmieder, B. 2006, JApA, 27, 139
Schmieder, B., Démoulin, P., & Aulanier, G. 2013, Adv. Space Res., 51, 1967
Schmieder, B., Aulanier, G., & Vršnak, B. 2015, Sol. Phys., 290, 3457
Schrijver, C. J., Kauristie, K., Aylward, A. D., et al. 2015, Adv. Space Res., 55, 2745
Shiota, D., Kusano, K., Miyoshi, T., & Shibata, K. 2010, ApJ, 718, 1305
Song, H. Q., Zhang, J., Chen, Y., & Cheng, X. 2014, ApJ, 792, L40
Song, H., Li, L., & Chen, Y. 2022, ApJ, 933, 68
Sturrock, P. A. 1966, Nature, 211, 695
Su, Y., Surges, V., van Ballegooijen, A., DeLuca, E., & Golub, L. 2011, ApJ, 734, 53
Tandberg-Hanssen, E. 1995, The nature of solar prominences (Dordrecht: Kluwer Academic Publishers)
Tandberg-Hanssen, E., & Malville, J. M. 1974, Sol. Phys., 39, 107
Thalmann, J. K., Dumbović, M., Dissauer, K., et al. 2023, A&A, 669, A72
Titov, V. S., Török, T., Mikic, Z., & Linker, J. A. 2014, ApJ, 790, 163
Titov, V. S., Downs, C., Mikić, Z., et al. 2018, ApJ, 852, L21
Tsurutani, B. T., Zank, G. P., Sterken, V. J., et al. 2023, IEEE Trans. Plasma Sci., 51, 1595
Verbeke, C., Pomoell, J., & Poedts, S. 2019, A&A, 627, A111
Vourlidas, A., Lynch, B. J., Howard, R. A., & Li, Y. 2013, Sol. Phys., 284, 179
Wang, Y., Zhou, G., Ye, P., Wang, S., & Wang, J. 2006, ApJ, 651, 1245
Wang, Y., Zhuang, B., Hu, Q., et al. 2016, J. Geophys. Res.: Space Phys., 121, 9316
Wang, W., Liu, R., Wang, Y., et al. 2017, Nat. Commun., 8, 1330
Wang, W., Zhu, C., Qiu, J., et al. 2019, ApJ, 871, 25
Wang, W., Qiu, J., Liu, R., et al. 2023, ApJ, 943, 80
Webb, D. F., Cliver, E. W., Crooker, N. U., Cry, O. C. S., & Thompson, B. J. 2000, J. Geophys. Res., 105, 7491
Webb, D. F., & Howard, T. A. 2012, Liv. Rev. Sol. Phys., 9, 3
Xing, C., Cheng, X., Qiu, J., et al. 2020a, ApJ, 889, 125
Xing, C., Cheng, X., & Ding, M. D. 2020b, The Innovation, 1, 100059
Xing, C., Aulanier, G., Schmieder, B., Cheng, X., Ding, M. 2024, A&A, 682, A3
Yurchyshyn, V. B., Wang, H., Goode, P. R., & Deng, Y. 2001, ApJ, 563, 381
Zhang, J., Richardson, I. G., Webb, D. F., et al. 2007, J. Geophys. Res.: Space Phys., 112, A10102
Zhang, J., Cheng, X., & Ding, M.-D. 2012, Nat. Commun., 3, 747
Zhang, Q., Wang, Y., Liu, R., et al. 2020, ApJ, 898, L12
Zhou, Z., Liu, R., Cheng, X., et al. 2020, ApJ, 891, 180
Zhou, Z., Jiang, C., Liu, R., et al. 2022, ApJ, 927, L14